

# XFOIL7 Full-Potential and Boundary Layer Formulation

Mark Drela

17 Feb 2017

## Nomenclature

$\mathbf{r}$	position ( $= x \hat{\mathbf{x}} + y \hat{\mathbf{y}}$ )	$\hat{\mathbf{n}}$	unit normal vector
$\mathbf{V}$	fluid velocity ( $= u \hat{\mathbf{x}} + v \hat{\mathbf{y}}$ )	$\hat{\mathbf{s}}$	unit tangential vector
$M$	Mach number	$\ell$	perimeter arc-length coordinate
$C_p$	pressure coefficient	$n$	wall-normal coordinate
$p$	static pressure	$s$	streamwise arc-length coordinate
$\rho$	density	$\xi, \eta$	finite-element coordinates
$\Phi$	full potential	$N_j(\xi, \eta)$	finite-element interpolation function
$\varphi$	perturbation potential	$W_i(\xi, \eta)$	finite-element residual weighting function
$\delta^*$	displacement thickness	$\alpha$	freestream flow angle
$\theta$	momentum thickness	$\Lambda$	farfield apparent source
$H$	shape parameter	$\Gamma$	farfield circulation
$H^*$	kinetic energy thickness shape parameter	$\kappa_x, \kappa_y$	farfield doublet components
$H^{**}$	density thickness shape parameter	$(\ )_\infty$	freestream quantity
$c_f$	skin friction coefficient	$(\ )_w$	body-wall or wake quantity
$c_D$	dissipation coefficient	$(\ )_e$	boundary layer edge quantity

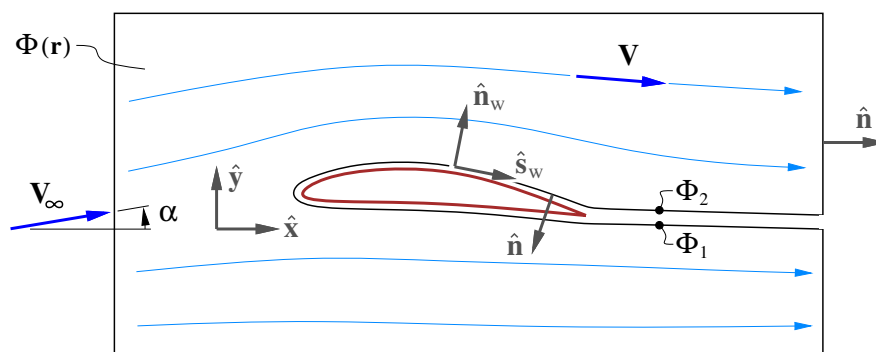


Figure 1: Potential flow domain.

## 1 Potential and Velocity

The velocity vector field is defined as the gradient of the full potential field  $\Phi(\mathbf{r})$ .

$$\mathbf{V}(\mathbf{r}) = \nabla \Phi \quad (1)$$

This is governed by the full-potential (FP) equation

$$\nabla \cdot [(\rho + \delta\rho) \nabla \Phi] = 0 \quad (2)$$

$$\rho = \rho_\infty \left[ 1 + \frac{\gamma-1}{2} M_\infty^2 \left( 1 - \frac{|\nabla \Phi|^2}{V_\infty^2} \right) \right]^{1/(\gamma-1)} \quad (3)$$

where the isentropic density expression (3) assumes a constant total density everywhere, and  $\delta\rho$  is its numerical upwinding change which will be formulated to enable shock capturing.

The appropriate boundary conditions, with wall-transpiration viscous modeling, are

$$\Phi = \Phi_\infty + \varphi_{\text{ff}} \quad (\text{outer boundary}) \quad (4)$$

$$\nabla\Phi \cdot \hat{\mathbf{n}}_w = dm/ds \quad (\text{body surface}) \quad (5)$$

where the freestream potential is specified in terms of the freestream speed and angle of attack.

$$\Phi_\infty = \mathbf{V}_\infty \cdot \mathbf{r} = V_\infty(x \cos \alpha + y \sin \alpha) \quad (6)$$

and  $m(s) = \rho_e u_e \delta^*$  is the viscous mass defect along the surface.

A body with lift requires that a branch cut with a potential jump extend from the body, which for an airfoil is most conveniently chosen to be roughly the wake trajectory from the trailing edge. Referring to Figure 1, the appropriate boundary conditions on the branch cut are

$$(\nabla\Phi \cdot \hat{\mathbf{n}}_w)_1 + (\nabla\Phi \cdot \hat{\mathbf{n}}_w)_2 = dm/ds \quad (7)$$

$$\Phi_2 - \Phi_1 = \Gamma \quad (8)$$

where  $\Gamma$  is the overall body circulation. Equation (8) in effect also imposes equal streamwise velocities and hence equal pressures across the branch cut.

## 2 Farfield Potential

The farfield perturbation potential  $\varphi_{\text{ff}}$  appears in the outer boundary condition (4) for external flows. It is a specific solution of the Prandtl-Glauert equation and outer boundary condition,

$$\beta^2 \frac{\partial^2 \varphi}{\partial x^2} + \frac{\partial^2 \varphi}{\partial y^2} = 0 \quad (9)$$

$$|\nabla\varphi| \rightarrow 0 \quad (\text{as } r \rightarrow \infty) \quad (10)$$

which is what remains when  $\Phi = \Phi_\infty + \varphi$  is substituted in the full-potential equation and BC, and only the terms which are first order in  $\nabla\varphi$  are retained. For subsonic freestream flow, or  $M_\infty < 1$ , the leading-order solution to (9) has the form

$$\varphi_{\text{ff}}(x, y; M_\infty, \alpha; \Lambda, \Gamma, \kappa_x, \kappa_y) = \frac{\Lambda}{2\pi} \ln \bar{r} - \frac{\Gamma}{2\pi} \bar{\theta} + \frac{\kappa_x}{2\pi} \frac{\cos \bar{\theta}}{\bar{r}} + \frac{\kappa_y}{2\pi} \frac{\sin \bar{\theta}}{\bar{r}} + \dots \quad (11)$$

$$\begin{Bmatrix} \bar{x} \\ \bar{y} \end{Bmatrix} \equiv \begin{bmatrix} \cos \alpha & \sin \alpha \\ -\beta \sin \alpha & \beta \cos \alpha \end{bmatrix} \begin{Bmatrix} x - x_s \\ y - y_s \end{Bmatrix} \quad (12)$$

$$\beta \equiv \sqrt{1 - M_\infty^2} \quad (13)$$

$$\bar{r}^2 \equiv \bar{x}^2 + \bar{y}^2 \quad (14)$$

$$\bar{\theta} \equiv \arctan(\bar{y}/\bar{x}) \quad (15)$$

where (12) is the Prandtl-Glauert coordinate transformation giving  $\bar{x}, \bar{y}$  aligned with the freestream. The singularity location  $x_s, y_s$  is chosen to be near or inside the body for best accuracy, and specifically to give the smallest-possible truncated terms in the expansion (11). The  $\Gamma$  (circulation) coefficient is required to produce lift. In contrast, the  $\Lambda$  (source) and  $\kappa_x, \kappa_y$  (doublet) terms can all

be set to zero which gives the simplest model, but defining them appropriately will give the best possible accuracy for a domain of given size.

The farfield velocity is most easily evaluated by differentiating in the transformed coordinates, and applying the inverse Prandtl-Glauert transformation.

$$\mathbf{V}_{\text{ff}} = \mathbf{V}_{\infty} + \nabla\varphi_{\text{ff}} \quad (16)$$

$$\nabla\varphi_{\text{ff}} = \begin{bmatrix} \cos \alpha & -\beta \sin \alpha \\ \sin \alpha & \beta \cos \alpha \end{bmatrix} \begin{Bmatrix} \partial\varphi_{\text{ff}}/\partial\bar{x} \\ \partial\varphi_{\text{ff}}/\partial\bar{y} \end{Bmatrix} \quad (17)$$

$$\frac{\partial\varphi_{\text{ff}}}{\partial\bar{x}} = \frac{\Lambda}{2\pi} \frac{\bar{x}}{\bar{r}^2} + \frac{\Gamma}{2\pi} \frac{\bar{y}}{\bar{r}^2} + \frac{\kappa_x}{2\pi} \frac{\bar{y}^2 - \bar{x}^2}{\bar{r}^4} + \frac{\kappa_y}{2\pi} \frac{-2\bar{x}\bar{y}}{\bar{r}^4} \quad (18)$$

$$\frac{\partial\varphi_{\text{ff}}}{\partial\bar{y}} = \frac{\Lambda}{2\pi} \frac{\bar{y}}{\bar{r}^2} + \frac{\Gamma}{2\pi} \frac{-\bar{x}}{\bar{r}^2} + \frac{\kappa_x}{2\pi} \frac{-2\bar{x}\bar{y}}{\bar{r}^4} + \frac{\kappa_y}{2\pi} \frac{\bar{x}^2 - \bar{y}^2}{\bar{r}^4} \quad (19)$$

Determination of the singularity strengths  $\Lambda, \Gamma, \kappa_x, \kappa_y$  will be treated later.

### 3 Finite-Element Full-Potential Solution

#### 3.1 Element Interpolation

A quadrilateral cell in  $x, y$  space is mapped to a reference cell in  $\xi, \eta$  space extending over  $(\xi, \eta) = (-1 \dots +1, -1 \dots +1)$ . Each field variable is then defined over the cell by its nodal values  $(\ )_j$  using the four bilinear interpolation functions  $N_j(\xi, \eta)$ ,

$$\begin{aligned} N_1(\xi, \eta) &\equiv \frac{1}{4}(1 - \xi)(1 - \eta) \\ N_2(\xi, \eta) &\equiv \frac{1}{4}(1 + \xi)(1 - \eta) \\ N_3(\xi, \eta) &\equiv \frac{1}{4}(1 + \xi)(1 + \eta) \\ N_4(\xi, \eta) &\equiv \frac{1}{4}(1 - \xi)(1 + \eta) \end{aligned} \quad (20)$$

$$x(\xi, \eta) = \sum_{j=1}^4 x_j N_j(\xi, \eta) \quad (21)$$

$$y(\xi, \eta) = \sum_{j=1}^4 y_j N_j(\xi, \eta) \quad (22)$$

$$\Phi(\xi, \eta) = \sum_{j=1}^4 \Phi_j N_j(\xi, \eta) \quad (23)$$

etc., where  $(\ )_j$  are the nodal variable values.

The mapping Jacobian  $J$  and the inverse mapping derivatives are now computed in the usual manner,

$$J(\xi, \eta) = x_{\xi} y_{\eta} - x_{\eta} y_{\xi} \quad (24)$$

$$\begin{bmatrix} \xi_x & \xi_y \\ \eta_x & \eta_y \end{bmatrix} (\xi, \eta) = \frac{1}{J} \begin{bmatrix} y_{\eta} & -x_{\eta} \\ -y_{\xi} & x_{\xi} \end{bmatrix} \quad (25)$$

where  $x_\xi$ ,  $y_\eta$ , etc. denote derivatives, which are obtained directly from (21) and (22). The inverse derivatives are then used to compute the  $x, y$ -components of the interpolation function gradient  $\nabla N_j = N_{x_j} \hat{\mathbf{x}} + N_{y_j} \hat{\mathbf{y}}$ .

$$N_{x_j}(\xi, \eta) = \xi_x N_{\xi_j} + \eta_x N_{\eta_j} \quad (26)$$

$$N_{y_j}(\xi, \eta) = \xi_y N_{\xi_j} + \eta_y N_{\eta_j} \quad (27)$$

where  $N_{\xi_j}$ ,  $N_{\eta_j}$  are obtained easily by differentiating (20). The gradient  $x, y$ -components of all interpolated quantities can then be obtained by direct summations.

$$\frac{\partial \Phi}{\partial x}(\xi, \eta) = \sum_{j=1}^4 \Phi_j N_{x_j} \quad (28)$$

$$\frac{\partial \Phi}{\partial y}(\xi, \eta) = \sum_{j=1}^4 \Phi_j N_{y_j} \quad (29)$$

### 3.2 Edge Interpolation

Interpolation over an element edge segment uses the two linear interpolation functions

$$\tilde{N}_1(\xi) \equiv \frac{1}{2}(1 - \xi) \quad (30)$$

$$\tilde{N}_2(\xi) \equiv \frac{1}{2}(1 + \xi)$$

together with the two nodal values  $(\ )_j$ , so that along the edge we have

$$x(\xi) = \sum_{j=1}^2 x_j \tilde{N}_j(\xi) \quad (31)$$

$$y(\xi) = \sum_{j=1}^2 y_j \tilde{N}_j(\xi) \quad (32)$$

$$\Phi(\xi) = \sum_{j=1}^2 \Phi_j \tilde{N}_j(\xi) \quad , \quad \text{etc.} \quad (33)$$

Arc length derivatives are given by direct chain rule,

$$\frac{d\Phi}{ds}(\xi) = \sum_{j=1}^2 \Phi_j \tilde{N}_{s_j} \quad (34)$$

$$\tilde{N}_{s_j} = \frac{d\tilde{N}_j/d\xi}{ds/d\xi} = \frac{\mp 1}{\sqrt{(x_2 - x_1)^2 + (y_2 - y_1)^2}} \quad (35)$$

where  $-1, +1$  give  $\tilde{N}_{s_1}, \tilde{N}_{s_2}$ . Equation (34) is equivalent to simple two-point finite differencing.

### 3.3 Galerkin Weighted-Residual Formulation

The Galerkin method chooses a weighting “tent” function  $W_i(\xi, \eta)$  for node  $i$  to be the union of the four, two, or one  $N_j$  interpolating functions influenced by that node, as shown in Figure 2.

Since the  $W_i(\xi, \eta)$  of nodes in the interior are zero on their edges, the edge integral around  $W_i$  for any interior node vanishes.

$$\oint \{ \} W_i \, dl = 0 \quad (\text{for interior nodes}) \quad (36)$$

For nodes on the domain outer boundary the edge  $W_i$  is not zero, and the cell-boundary integral (36) will be evaluated using appropriate boundary condition information.

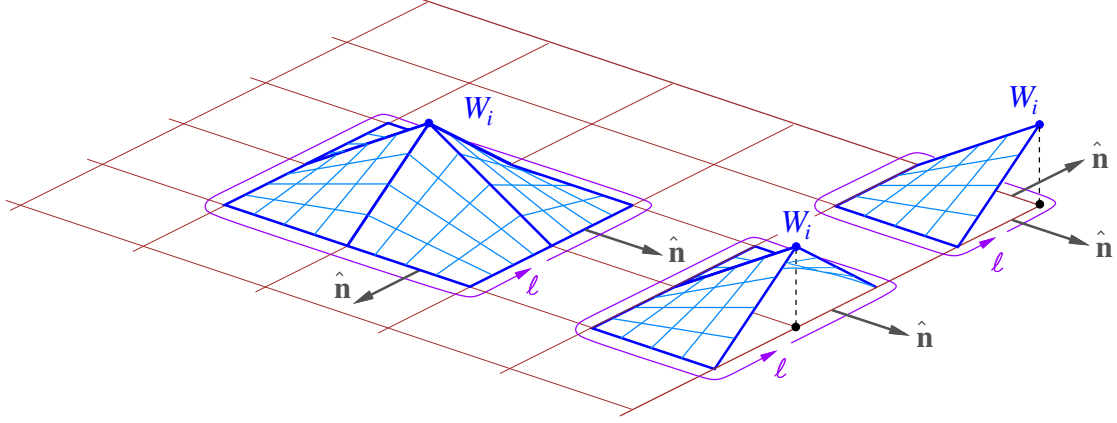


Figure 2: Residual weighting tent function  $W_i$  for interior, edge, and corner nodes.

A weighted-residual integration of the full-potential equation (2) is constructed and expanded as

$$\mathcal{R}_i^\Phi(\Phi) \equiv \iint \nabla \cdot [(\rho + \delta\rho) \nabla \Phi] W_i \, dx \, dy \quad (37)$$

$$\begin{aligned} &= \iint \nabla \cdot [(\rho + \delta\rho) \nabla \Phi W_i] \, dx \, dy - \iint (\rho + \delta\rho) \nabla \Phi \cdot \nabla W_i \, dx \, dy \\ &= \oint (\rho + \delta\rho) \nabla \Phi \cdot \hat{\mathbf{n}} W_i \, d\ell - \iint (\rho + \delta\rho) \nabla \Phi \cdot \nabla W_i \, dx \, dy = 0 \end{aligned} \quad (38)$$

where the first term in (38) has then been converted to a cell-boundary line integral via Gauss's Theorem. The integrals need to be evaluated over only those edges and cells on which  $W_i$  is nonzero.

Writing  $\nabla \Phi$  in (38) in its interpolated forms (28),(29), the area integral in (38) becomes

$$\iint (\rho + \delta\rho) \nabla \Phi \cdot \nabla W_i \, dx \, dy = \sum_{\text{elements}} (\rho + \delta\rho) \sum_j \Phi_j \iint (N_{x_j} W_{x_i} + N_{y_j} W_{y_i}) \, dx \, dy \quad (39)$$

where the first sum is over the elements covered by  $W_i$ , and the second sum is over the four nodes of each element. The upwinded density factor  $(\rho + \delta\rho)$  is constant over each element, and will be discussed and defined later.

The line integral in (38) is typically evaluated using boundary information for boundary nodes such as on the body, where a Neumann boundary condition is imposed.

$$\oint (\rho + \delta\rho) \nabla \Phi \cdot \hat{\mathbf{n}} W_i \, d\ell = \begin{cases} 0 & , \text{ (for interior node } i) \\ \int -[(\rho + \delta\rho) \nabla \Phi \cdot \hat{\mathbf{n}}_w]_{\text{BC}} W_i \, ds & , \text{ (for boundary node } i) \end{cases} \quad (40)$$

The negative sign in (40) is needed because  $\hat{\mathbf{n}}$  points out of the fluid while  $\hat{\mathbf{n}}_w$  points out of the body, as indicated in Figure 1. Possible values for the boundary data are

$$[(\rho + \delta\rho) \nabla \Phi \cdot \hat{\mathbf{n}}_w]_{\text{BC}} = \begin{cases} 0 & , \text{ (for solid wall)} \\ \frac{dm}{ds} & , \text{ (for wall-transpiration viscous model)} \end{cases} \quad (41)$$

where  $m = \rho_e u_e \delta^*$  is the viscous mass defect and  $s$  is the streamwise arc length along the wall.

For boundary nodes where a Dirichlet boundary condition is imposed, the residual (37) is replaced by a direct condition on the potential.

$$\mathcal{R}_i^\Phi \equiv \int [\Phi - \Phi_{\text{BC}}] W_i \, ds = 0 \quad (42)$$

Possible values for the boundary data are

$$\Phi_{\text{BC}} = \begin{cases} \Phi_\infty + \varphi_{\text{ff}} & , \text{ (for outer boundary)} \\ \Phi_{\text{spec}} & , \text{ (for inverse-design wall)} \end{cases} \quad (43)$$

where  $\Phi_{\text{spec}}(s) = \int^s q_{\text{spec}} \, ds$  is the potential obtained from a specified surface speed  $q_{\text{spec}}(s)$  or corresponding surface pressure in an inverse-design calculation.

The branch cut boundary conditions (7) and (8) are implemented by the residuals

$$\mathcal{R}_{i_1}^\Phi \equiv \int (\rho + \delta\rho) \nabla\Phi \cdot \hat{\mathbf{n}}_1 W_{i_1} \, ds_1 + \int (\rho + \delta\rho) \nabla\Phi \cdot \hat{\mathbf{n}}_2 W_{i_2} \, ds_2 + \int \frac{dm}{ds} W_i \, ds = 0 \quad (44)$$

$$\mathcal{R}_{i_2}^\Phi \equiv \int \Phi W_{i_1} \, ds_1 - \int [\Phi - \Gamma] W_{i_2} \, ds_2 = 0 \quad (45)$$

where the circulation  $\Gamma$  is the same quantity appearing in the far-field potential  $\varphi_{\text{ff}}$  expansion (11).

### 3.4 Element-Integral Evaluation

The element area integrals needed to construct all the equation residuals are evaluated using a 4-point Gaussian area quadrature on the  $\xi$ - $\eta$  cell,

$$\iint \{ \} \, dx \, dy = \int_{-1}^1 \int_{-1}^1 \{ \} \, J \, d\xi \, d\eta \simeq \sum_{k=1}^4 \{ \}_{(\xi_k, \eta_k)} J(\xi_k, \eta_k) w_k \quad (46)$$

where  $(\xi_k, \eta_k)$  are the Gauss-point locations, and  $w_k$  are the corresponding Gauss weights.

The  $(\rho + \delta\rho)$  density factor appearing in the various weighted integrals above can be assumed to be constant over each of the individual quadrilateral cells. The reason is that  $\Phi(\xi, \eta)$  is bilinear over a cell, so that  $\nabla\Phi(\xi, \eta)$  and the corresponding  $\rho(\xi, \eta)$  are nearly constant. Specifically, the cell  $\rho$  value is obtained from (3) using  $\nabla\Phi$  computed at the cell center at  $(\xi, \eta) = (0, 0)$  rather than at the Gauss points. The area integral in (38) and (39) over one cell is then evaluated as follows.

$$\iint (\rho + \delta\rho) \nabla\Phi \cdot \nabla W_i \, dx \, dy \simeq (\rho + \delta\rho)_{(0,0)} \sum_{k=1}^4 \{ \nabla\Phi \cdot \nabla W_i \}_{(\xi_k, \eta_k)} J(\xi_k, \eta_k) w_k \quad (47)$$

$$\xi_k, \eta_k = \pm\sqrt{1/3} = \pm 0.577350269189626 \quad (48)$$

$$w_k = 1 \quad (49)$$

Evaluating  $\nabla\Phi \cdot \nabla W_i$  at the four Gauss points  $(\xi_k, \eta_k)$  makes spatial sawtooth oscillations in  $\Phi_i$  visible to  $\mathcal{R}_i^\Phi$ , thus producing a well-conditioned overall Jacobian matrix.

The element boundary integrals are evaluated using 2-point Gaussian line quadrature on the  $\xi$  or  $\eta$  boundary.

$$\oint \{ \} \, dl = \oint \{ \} \, J \, d\xi \simeq \sum_{k=1}^2 \{ \}_{(\xi_k)} J(\xi_k) w_k \quad (50)$$

With linear interpolation, the Jacobian is actually piecewise constant along each cell edge segment, and over each segment simplifies to

$$J = \frac{\Delta\ell}{\Delta\xi} = \frac{\Delta\ell}{2} \quad (51)$$

where  $\Delta\ell$  is the length of the segment.

### 3.5 Global-Variable Equations

The freestream angle of attack  $\alpha$ , Mach number  $M_\infty$ , and the farfield potential coefficients  $\Lambda, \Gamma, \kappa_x, \kappa_y$  appear in many or all node residuals. Hence, they are called *global variables*, and each one requires an additional residual to close the overall system. Possible constraints on the angle of attack are

$$\mathcal{R}^\alpha \equiv \alpha - \alpha_{\text{spec}} = 0 \quad (\text{specified angle of attack}) \quad (52)$$

$$\mathcal{R}^\alpha \equiv C_L - C_{L\text{spec}} = 0 \quad (\text{specified lift coefficient}) \quad (53)$$

where the lift coefficient can be replaced by the circulation via the theoretically exact relation  $C_L = 2\Gamma/cV_\infty$ . In the numerical solution there will be some small difference due to truncation error.

The Mach number can also be imposed directly, or it can depend on the lift coefficient,

$$\mathcal{R}^M \equiv M_\infty - M_{\infty\text{spec}} = 0 \quad (\text{specified Mach number}) \quad (54)$$

$$\mathcal{R}^M \equiv M_\infty - M_{\infty 1}/\sqrt{C_L} = 0 \quad (\text{specified unit-lift Mach number})(55)$$

where the unit- $C_L$  Mach number  $M_{\infty 1}$  is specified and held fixed. This case corresponds to the physical lift remaining fixed as the airspeed is varied at a fixed altitude. For viscous-flow cases, the same type of fixed-lift condition can be imposed on the Reynolds number in the form

$$Re = Re_1/\sqrt{C_L} \quad (56)$$

where the unit- $C_L$  Reynolds number  $Re_1$  is specified explicitly.

The physically-appropriate constraint on the circulation is the Kutta condition, which is defined as the difference between the top and bottom surface pressures at the trailing edge.

$$\mathcal{R}^\Gamma \equiv p_{i_{TE_2}} - p_{i_{TE_1}} = 0 \quad (57)$$

A simpler alternative definition is to impose the wake branch-cut jump condition (45) pointwise at the wake station also.

$$\mathcal{R}^\Gamma \equiv \Phi_{i_{TE_1}} - \Phi_{i_{TE_2}} - \Gamma = 0 \quad (58)$$

The farfield source and doublet strengths can be set to zero via the simple residuals

$$\mathcal{R}^\Lambda \equiv \Lambda = 0 \quad (59)$$

$$\mathcal{R}^{\kappa_x} \equiv \kappa_x = 0 \quad (60)$$

$$\mathcal{R}^{\kappa_y} \equiv \kappa_y = 0 \quad (61)$$

which will give a well-posed problem and a reasonable solution.

A more accurate solution, especially on modest-sized grids, will be obtained if we instead set the strengths so as to give the best possible match between the normal derivatives of  $\Phi_\infty + \varphi_{\text{ff}}$  and  $\Phi$  at the outer boundary. To impose this, we first define the normal-derivative mismatch (or error) functional

$$\mathcal{I}_\infty \equiv \oint \frac{1}{2} [(\mathbf{V}_\infty + \nabla\varphi_{\text{ff}}) \cdot \hat{\mathbf{n}} - \nabla\Phi \cdot \hat{\mathbf{n}}]^2 dl \quad (62)$$

where the integral is evaluated over the entire outer boundary. The farfield strengths are then set so that this functional is minimized, via the following residuals.

$$\mathcal{R}^\Lambda \equiv \frac{\partial \mathcal{I}_\infty}{\partial \Lambda} = \oint [(\mathbf{V}_\infty + \nabla\varphi_{\text{ff}}) \cdot \hat{\mathbf{n}} - \nabla\Phi \cdot \hat{\mathbf{n}}] \frac{\partial \nabla\varphi_{\text{ff}}}{\partial \Lambda} \cdot \hat{\mathbf{n}} dl = 0 \quad (63)$$

$$\mathcal{R}^{\kappa_x} \equiv \frac{\partial \mathcal{I}_\infty}{\partial \kappa_x} = \oint [(\mathbf{V}_\infty + \nabla\varphi_{\text{ff}}) \cdot \hat{\mathbf{n}} - \nabla\Phi \cdot \hat{\mathbf{n}}] \frac{\partial \nabla\varphi_{\text{ff}}}{\partial \kappa_x} \cdot \hat{\mathbf{n}} dl = 0 \quad (64)$$

$$\mathcal{R}^{\kappa_y} \equiv \frac{\partial \mathcal{I}_\infty}{\partial \kappa_y} = \oint [(\mathbf{V}_\infty + \nabla\varphi_{\text{ff}}) \cdot \hat{\mathbf{n}} - \nabla\Phi \cdot \hat{\mathbf{n}}] \frac{\partial \nabla\varphi_{\text{ff}}}{\partial \kappa_y} \cdot \hat{\mathbf{n}} dl = 0 \quad (65)$$

The derivatives  $\partial \nabla\varphi_{\text{ff}}/\partial \Lambda$ ,  $\partial \nabla\varphi_{\text{ff}}/\partial \kappa_x$ ,  $\partial \nabla\varphi_{\text{ff}}/\partial \kappa_y$  are purely geometric quantities obtained directly from equations (17)–(19). Hence, the residuals above are nearly linear in the strengths  $\Lambda$ ,  $\kappa_x$ ,  $\kappa_y$  via the  $\nabla\varphi_{\text{ff}} \cdot \hat{\mathbf{n}}$  term, giving a well-posed set of constraint equations for these quantities.

Note that  $\Gamma$  could not have been obtained in this manner by minimizing  $\mathcal{I}_\infty$  with respect to  $\Gamma$ , since  $\partial \nabla\varphi_{\text{ff}}/\partial \Gamma$  is tangential to a circle around the  $x_s, y_s$  location at the airfoil. The consequence is that

$$\frac{\partial \nabla\varphi_{\text{ff}}}{\partial \Gamma} \cdot \hat{\mathbf{n}} \simeq 0$$

on average over the outer boundary, so that a minimum-error residual for  $\Gamma$  having the same form as (63)–(65) would be a nearly-singular equation. The Kutta condition (58) is therefore the appropriate constraint on  $\Gamma$  for both physical and computational reasons.

### 3.6 Density Upwinding

Some form of upwinding is required to give a non-singular full-potential equation Jacobian at sonic points, and to permit shock capturing in the solution. The treatment here computes the density upwinding change by

$$\delta\rho = -\mu_1(\rho_i - \rho_{i-1}) + \mu_2(\rho_{i-1} - \rho_{i-2}) \frac{\Delta s_{i-1/2}}{\Delta s_{i-3/2}} \quad (66)$$

$$\mu_1 = C_\mu \max\left(0, 1 - \frac{M_{\text{crit}}^2}{M_{\text{max}}^2}\right) \quad (67)$$

$$\mu_2 = \begin{cases} 0 & \text{if 1st-order upwinding is specified} \\ \mu_1 & \text{if 2nd-order upwinding is specified} \end{cases} \quad (68)$$

$$M_{\text{max}}^2 = \max(M_i^2, M_{i-1}^2) \quad (69)$$

$$\Delta s_{i-1/2} = |\mathbf{r}_i - \mathbf{r}_{i-1}| \quad (70)$$

$$\Delta s_{i-3/2} = |\mathbf{r}_{i-1} - \mathbf{r}_{i-2}| \quad (71)$$

where here  $i$  denotes a cell center at  $(\xi, \eta) = (0, 0)$ , and not a node at  $(\pm 1, \pm 1)$ . The  $i-2, i-1, i$  cell centers are assumed to lie along the local  $\nabla\Phi$  direction. For a general grid this requires interpolation

between neighboring cell centers, which constitutes Jameson’s rotated-difference scheme. In this description we will assume that the grid increasing- $i$  direction is nearly aligned with  $\nabla\Phi$ .

The first  $\mu_1$  term in equation (66) is Hafez’s 1st-order upwinding scheme, and the optional  $\mu_2$  term is a density-extrapolation correction which restores 2nd-order accuracy. The two forms are diagrammed in Figure 3.

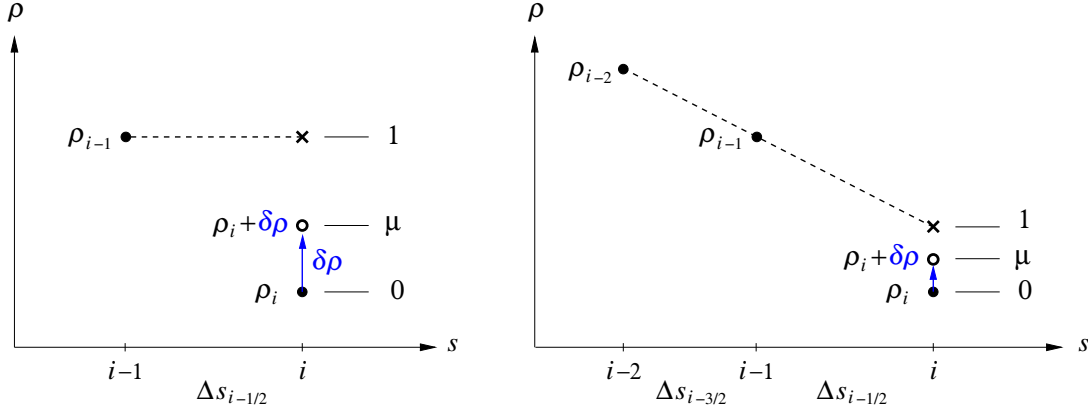


Figure 3: Density upwinding change  $\delta\rho$  using 1st-order and 2nd-order schemes. The index  $i$  here indicates cell centers rather than nodes. In each case,  $\delta\rho$  is the fraction  $\mu$  of the difference between the density extrapolated from the upstream  $i-1$  and/or  $i-2$  locations, and the local density at  $i$ .

Suitable values for the constants in (66) are

$$M_{\text{crit}} \simeq 0.98 \quad (72)$$

$$C_\mu \simeq 1.0 \quad (73)$$

which were obtained by numerical experimentation. Theoretically,  $C_\mu = 0.5$  will still give a numerically stable scheme and the sharpest possible shock, provided the shock is perfectly aligned with the grid lines. For non-aligned shocks, the values above generally give better results.

### 3.7 Newton Solution Method

For inviscid flow, the unknowns in the discrete problem are the local full potential values  $\Phi_i$  at all the grid nodes, and the six global variables

$$g_k \equiv \left\{ \alpha \quad M_\infty \quad \Lambda \quad \Gamma \quad \kappa_x \quad \kappa_y \right\}^T$$

associated with the entire flowfield. The entire equation system then has the form

$$\vec{\mathcal{R}}_{(\Phi_j, g_l)} \equiv \begin{Bmatrix} \mathcal{R}_i^\Phi \\ \mathcal{R}_k^g \end{Bmatrix} = \mathbf{0} \quad (74)$$

where

$$\mathcal{R}_k^g \equiv \left\{ \mathcal{R}^\alpha \quad \mathcal{R}^M \quad \mathcal{R}^\Lambda \quad \mathcal{R}^\Gamma \quad \mathcal{R}^{\kappa_x} \quad \mathcal{R}^{\kappa_y} \right\}^T$$

is the vector of global residual functions.

The residuals are in general nonlinear functions of the unknowns, so a direct solution of the equation set (74) is not possible. Instead, the problem is solved by *Newton iteration*, where we obtain a sequence of progressively-better solution iterates

$$\{\Phi_i \ g_k\}^0, \{\Phi_i \ g_k\}^1, \{\Phi_i \ g_k\}^2 \dots \{\Phi_i \ g_k\}^n$$

where  $n$  is the iteration counter and  $n=0$  is some reasonable initial guess for the solution, such as freestream flow for  $\Phi_i$ , and either zeros or specified values (if available) for the global variables.

$$\{\Phi_i \ g_k\}^0 = \{\Phi_{\infty_i} \ \mathbf{0}\}$$

Given some current solution iterate  $n$ , we calculate the *Newton changes*  $\{\delta\Phi_i \ \delta g_k\}$  which when added to the iterate  $n$  give the next iterate  $n+1$ . The requirement for these changes is that the residual vector is zero after the update, i.e.

$$\vec{\mathcal{R}}(\Phi_i^{n+1}, g_k^{n+1}) = \vec{\mathcal{R}}(\Phi_i^n + \delta\Phi_i, g_k^n + \delta g_k) = \mathbf{0}.$$

Because this is a nonlinear system, we linearize it about the current iterate to give

$$\vec{\mathcal{R}}(\Phi_i^n + \delta\Phi_i, g_k^n + \delta g_k) \simeq \begin{Bmatrix} \mathcal{R}_i^\Phi \\ \mathcal{R}_k^g \end{Bmatrix}^n + \left[ \begin{array}{c|c} A_{ij} & C_{il} \\ \hline G_{kj} & K_{kl} \end{array} \right]^n \begin{Bmatrix} \delta\Phi_j \\ \delta g_l \end{Bmatrix} = \mathbf{0} \quad (75)$$

where the rightmost residual vector and the leftmost *Jacobian matrix* is formed from the four submatrices

$$A_{ij} \equiv \left. \frac{\partial \mathcal{R}_i^\Phi}{\partial \Phi_j} \right|_{\{\Phi_i \ g_k\}^n}, \quad C_{il} \equiv \left. \frac{\partial \mathcal{R}_i^\Phi}{\partial g_l} \right|_{\{\Phi_i \ g_k\}^n} \quad (76)$$

$$G_{kj} \equiv \left. \frac{\partial \mathcal{R}_k^g}{\partial \Phi_j} \right|_{\{\Phi_i \ g_k\}^n}, \quad K_{kl} \equiv \left. \frac{\partial \mathcal{R}_k^g}{\partial g_l} \right|_{\{\Phi_i \ g_k\}^n} \quad (77)$$

are all evaluated at the current solution iterate  $\{\Phi_i \ g_k\}^n$  as indicated. With the residual vector and the matrix known numerically, equation (75) is a large *linear* system which can be solved for the unknown Newton changes.

$$\begin{Bmatrix} \delta\Phi_j \\ \delta g_l \end{Bmatrix} = \left[ \begin{array}{c|c} A_{ij} & B_{il} \\ \hline C_{kj} & D_{kl} \end{array} \right]^{-1} \begin{Bmatrix} -\mathcal{R}_i^\Phi \\ -\mathcal{R}_k^g \end{Bmatrix} \quad (78)$$

In practice, in place of the matrix inverse we would instead perform a LU-decomposition of the matrix, followed by a back-substitution with the residual vector. Since each  $\mathcal{R}_i^\Phi$  function depends on only a few neighboring  $\Phi_j$  values, the largest  $A_{ij}$  block of the Jacobian matrix is very *sparse*, so that we can also use various iterative methods to solve the linear system (75).

Regardless of the solution procedure, the Newton changes obtained are used to update the current solution iterate to give the next iterate,

$$\begin{pmatrix} \Phi_j \\ \hline g_l \end{pmatrix}^{n+1} = \begin{pmatrix} \Phi_j \\ \hline g_l \end{pmatrix}^n + \omega \begin{pmatrix} \delta\Phi_j \\ \hline \delta g_l \end{pmatrix} \quad (79)$$

where  $\omega \leq 1$  is a *limiter* or *under-relaxation factor*. This is necessary to prevent excessive changes which may produce unphysical situations such as a negative density in the  $n+1$  solution iterate. Once the changes become sufficiently small we can set  $\omega = 1$ , and as the solution is approached we observe *quadratic convergence*, i.e.

$$\left| \delta\Phi_i^{n+1} \delta g_k^{n+1} \right| \sim \left| \delta\Phi_i^n \delta g_k^n \right|^2 \quad (80)$$

so that the number of converged significant digits in the iterates roughly doubles with each iteration.

### 3.8 Field Velocity Calculation

The velocity components are approximated over each cell via their nodal values  $u_j, v_j$  using the bilinear interpolation functions.

$$\begin{aligned} u(\xi,\eta) &= \sum_j u_j N_j(\xi,\eta) \\ v(\xi,\eta) &= \sum_j v_j N_j(\xi,\eta) \end{aligned} \quad (81)$$

Once the finite-element problem is solved for  $\Phi_j$ , the corresponding nodal velocities  $u_j$  and  $v_j$  are determined by applying the velocity-potential definition (1) in weighted-integral form.

$$\begin{aligned} \iint u W_i \, dx \, dy &= \iint \frac{\partial\Phi}{\partial x} W_i \, dx \, dy \\ \iint v W_i \, dx \, dy &= \iint \frac{\partial\Phi}{\partial y} W_i \, dx \, dy \end{aligned} \quad (82)$$

The  $u, v, \Phi_x, \Phi_y$  inside the integrals above are approximated using the bilinear interpolation as usual. Carrying out the integrations gives the following linear systems for  $u_j$  and  $v_j$ .

$$\begin{aligned} M_{ij} u_j &= b_{u_i} \\ M_{ij} v_j &= b_{v_i} \end{aligned} \quad (83)$$

$$M_{ij} \equiv \iint N_j W_i \, dx \, dy \quad (84)$$

$$b_{u_i} \equiv \sum_j \Phi_j \iint N_{x_j} W_i \, dx \, dy \quad (85)$$

$$b_{v_i} \equiv \sum_j \Phi_j \iint N_{y_j} W_i \, dx \, dy$$

The node velocities are obtained from (83), by direct solution, via LU-factorization of the mass matrix  $M_{ij}$  and its back-substitution with the  $b_i$  vectors.

$$\begin{aligned} u_i &= M_{ij}^{-1} b_{u_i} \\ v_i &= M_{ij}^{-1} b_{v_i} \end{aligned} \quad (86)$$

Since  $M_{ij}$  depends only on the grid geometry, the LU-factorization which is the most expensive part of this calculation needs to be performed only once for any given grid. The velocities for any solution on that grid can then be obtained from the relatively fast back-substitution operations (86). Alternatively, the linear systems (83) can be solved iteratively.

### 3.9 Surface Velocity Calculation

One feature of equations (86) is that they make the velocity at one grid point depend on the potential at all the grid nodes (however weakly for distant points). This is inconsequential for post-processing, but it's not practical if the node velocities are needed in the equation residuals themselves. One example is when the boundary layer equations are solved in a fully coupled manner with the full potential equation, and the boundary-layer equation residuals are functions of the edge velocity

$$u_e = \hat{\mathbf{s}}_w \cdot \nabla \Phi \quad (87)$$

$$\hat{\mathbf{s}}_w = s_x \hat{\mathbf{x}} + s_y \hat{\mathbf{y}} \quad (88)$$

where  $\hat{\mathbf{s}}_w$  is the body-surface tangential unit vector. In this case we define the nodal edge velocity  $u_{e_i}$  along the surface, and compute them by expressing (87) in a weighted-integral form,

$$\int u_e \widetilde{W}_i ds = \int \frac{\partial \Phi}{\partial s} \widetilde{W}_i ds \quad (89)$$

which is a one-dimensional version of equations (82), with  $\widetilde{W}_i$  being a one-dimensional ‘‘tent’’ function of arc length along the surface, centered on node  $i$ . Equivalently,  $\widetilde{W}_i$  is the union of the two  $\widetilde{N}$  functions associated with that node on the adjacent elements.

Substituting the interpolated expressions for  $u_e$  and  $\partial \Phi / \partial s$  in (82) using the one-dimensional bilinear functions  $\widetilde{N}_j$ , and rearranging, gives the equivalent defining residual.

$$\mathcal{R}_i^u \equiv \sum_j u_{e_j} \int \widetilde{N}_j \widetilde{W}_i ds - \sum_j \Phi_j \int \widetilde{N}_{s_j} \widetilde{W}_i ds = 0 \quad (90)$$

When the full-potential equation is solved together with the integral boundary layer equations in a full-coupled manner, the nodal  $u_{e_i}$  become additional unknowns in the problem, and (90) become their corresponding additional residuals.

### 3.10 Pressure And Overall Force Calculation

The node pressure and pressure coefficient values are obtained directly from the isentropic pressure-velocity relation.

$$p_i = p_\infty \left[ 1 + \frac{\gamma-1}{2} M_\infty^2 \left( 1 - \frac{u_i^2 + v_i^2}{V_\infty^2} \right) \right]^{\gamma/(\gamma-1)} \quad (91)$$

$$C_{p_i} = \frac{2}{\gamma M_\infty^2} \left( \frac{p_i}{p_\infty} - 1 \right) \quad (92)$$

The overall forces and moment are then obtained by integration of these components around the body perimeter, performed counterclockwise.

$$C_x = \frac{1}{c} \oint_{\text{body}} -C_p dy \quad (93)$$

$$C_y = \frac{1}{c} \oint_{\text{body}} C_p \, dx \quad (94)$$

$$C_m = \frac{1}{c^2} \oint_{\text{body}} -C_p (x \, dx + y \, dy) \quad (95)$$

The pressure-drag coefficient and lift coefficient are the force components along and normal to the freestream direction.

$$C_{D_p} = C_x \cos \alpha + C_y \sin \alpha \quad (96)$$

$$C_L = C_y \cos \alpha - C_x \sin \alpha \quad (97)$$

## 4 Boundary Layer Formulation

### 4.1 Integral Boundary Layer Equations

In XFOIL7, the boundary layer evolution is governed by the integral boundary layer equations,

$$\frac{d\theta}{ds} = \frac{c_f}{2} - (H + 2 - M_e^2) \frac{\theta}{u_e} \frac{du_e}{ds} \quad (98)$$

$$\frac{\theta}{H^*} \frac{dH^*}{ds} = \frac{2c_D}{H^*} - \frac{c_f}{2} + \left( H - 1 - \frac{2H^{**}}{H^*} \right) \frac{\theta}{u_e} \frac{du_e}{ds} \quad (99)$$

which are the standard von Karman momentum equation and the kinetic energy shape parameter equation. In laminar portions we have the  $e^n$  envelope growth or amplification equation,

$$\frac{d\tilde{n}}{ds} = \frac{1}{\theta} \mathcal{F}_n(H_k, Re_\theta) \quad (100)$$

where  $\mathcal{F}_n$  is the amplification function which predicts the growth of TS wave amplitude growth. The transition point is the  $s$  location where the N-factor variable  $\tilde{n}(s)$  reaches a specified  $n_{\text{crit}}$  value, and is where the changeover from laminar to turbulent correlation functions is made.

In turbulent portions we have the shear lag equation

$$\frac{\delta}{C_\tau} \frac{dC_\tau}{ds} = K_C \left( C_{\tau_{EQ}}^{1/2} - C_\tau^{1/2} \right) + U'_{EQ} - \left( \frac{\delta}{u_e} \frac{du_e}{ds} \right) \quad (101)$$

which captures the relatively slow adjustment of the outer-layer Reynolds shear stress to the fluid's local strain rate.

### 4.2 Variables and Correlations

For coupled viscous/inviscid problems, the primary unknowns are the full-potential field  $\Phi(\mathbf{r})$ , and the following four boundary layer variables defined along the body surface and trailing wake.

$$\tilde{n}(s) \text{ or } C_\tau^{1/2}(s), \theta(s), m(s), u_e(s)$$

From these, the following secondary variables are defined.

$$\mathcal{T} = 1 + \frac{\gamma-1}{2} M_\infty^2 \left( 1 - \frac{u_e^2}{V_\infty^2} \right) \quad (102)$$

$$\rho_e = \rho_\infty \mathcal{T}^{1/(\gamma-1)} \quad (103)$$

$$\mu_e = \frac{\rho_\infty V_\infty \ell_{\text{ref}}}{Re_\infty} \mathcal{T}^{3/2} \frac{1+\mathcal{T}_S}{\mathcal{T}+\mathcal{T}_S} \quad ; \quad \mathcal{T}_S = 110 \text{ K}/T_\infty \quad (104)$$

$$M_e^2 = M_\infty^2 \frac{u_e^2}{V_\infty^2} \mathcal{T}^{-1} \quad (105)$$

$$\delta^* = \frac{m}{\rho_e u_e} \quad (106)$$

$$Re_\theta = \frac{\rho_e u_e \theta}{\mu_e} \quad (107)$$

$$H = \frac{\delta^*}{\theta} \quad (108)$$

$$H_k = \tilde{H}_k(H, M_e) \quad (109)$$

$$H^* = \tilde{H}^*(H, M_e) \quad (110)$$

$$H^{**} = \tilde{H}^{**}(H, M_e) \quad (111)$$

$$c_f = \tilde{c}_f(H, Re_\theta, M_e) \quad (112)$$

$$c_{\mathcal{D}} = \tilde{c}_{\mathcal{D}}(H, Re_\theta, M_e, C_\tau^{1/2}) \quad (113)$$

$$\delta = \tilde{\delta}(H_k, \theta) \quad (114)$$

$$C_{\tau_{EQ}}^{1/2} = \tilde{C}_{\tau_{EQ}}^{1/2}(H_k, Re_\theta, M_e) \quad (115)$$

$$U'_{EQ} = \tilde{U}'_{EQ}(H_k, Re_\theta) \quad (116)$$

The functions in definitions (109)–(116) are correlations obtained from assumed profile families  $u^{(n)}/u_e$ , and have laminar and turbulent versions. For the laminar correlations we use the Falkner-Skan profiles, and for the turbulent correlations profiles we use the Coles log layer plus wake layer composite profile. Minor modifications are performed for strongly separated profiles, mainly to limit the magnitude of the reverse velocities. The assumed density profile  $\rho^{(n)}/\rho_e$  used to construct the correlations is based on the Crocco-Busemann enthalpy profile, together with the usual approximation of a constant static pressure across the boundary layer. An adiabatic wall is also assumed. The G-beta equilibrium flow concept of Clauser is also used to construct the dissipation correlation function in (113). Finally, normalized pressure gradient function in (116) is obtained by applying the lag equation (which itself follows from the shear stress transport model of Bradshaw) to the G-beta equilibrium flow case.

## 4.3 Discretization

### 4.3.1 Equations

All boundary layer variables are defined at the surface nodes. We then define convenient variable averages over a node interval  $i-1 \dots i$  along the surface.

$$(\ )_a \equiv \frac{1}{2} \left[ (\ )_i + (\ )_{i-1} \right] \quad (117)$$

The equations are put into fractional differential residual form, for example

$$\frac{d\theta}{\theta} - \frac{s}{\theta} \frac{c_f}{2} \frac{ds}{s} + \left( H + 2 - M_e^2 \right) \frac{du_e}{u_e} = 0 \quad (118)$$

and then integrated over each interval. This gives the following discrete residuals.

$$\mathcal{R}_i^\theta \equiv \ln \frac{\theta_i}{\theta_{i-1}} - \left( \frac{s c_f}{\theta} \right)_a \ln \frac{s_i}{s_{i-1}} + (H_a + 2 - M_a^2) \ln \frac{u_{e_i}}{u_{e_{i-1}}} = 0 \quad (119)$$

$$\mathcal{R}_i^H \equiv \ln \frac{H_i^*}{H_{i-1}^*} - \left[ \left( \frac{s c_f}{\theta} \right)_a - \left( \frac{s 2c_D}{\theta H^*} \right)_a \right] \ln \frac{s_i}{s_{i-1}} + \left( H_a - 1 - \frac{2H_a^{**}}{H_a^*} \right) \ln \frac{u_{e_i}}{u_{e_{i-1}}} = 0 \quad (120)$$

$$\mathcal{R}_i^\tau \equiv \ln \frac{C_{\tau_i}}{C_{\tau_{i-1}}} - K_C \left[ \left( C_{\tau_{EQ}}^{1/2} \right)_a - \left( C_\tau^{1/2} \right)_a \right] \frac{s_i - s_{i-1}}{\theta_a} - \left( U'_{EQ} \right)_a \frac{s_i - s_{i-1}}{\theta_a} + \ln \frac{u_{e_i}}{u_{e_{i-1}}} = 0 \quad (121)$$

$$\mathcal{R}_i^n \equiv \tilde{n}_i - \tilde{n}_{i-1} - \frac{s_i - s_{i-1}}{\theta_a} \mathcal{F}_n(H_{k_a}, Re_{\theta_a}) = 0 \quad (122)$$

The edge velocity variable  $u_{e_i}$  is governed by the residual  $\mathcal{R}_i^u$ , given earlier in equation (90).

In equations (119) and (120), each of the variable combinations

$$\frac{s c_f}{\theta} \quad , \quad \frac{s 2c_D}{\theta H^*}$$

is averaged as a group as indicated. The reason is that these groups always asymptote to a constant value towards the leading edge or stagnation point at  $s=0$  for any self-similar flow (e.g. Blasius, stagnation point, etc.), while  $c_f$  and  $c_D$  are always singular there. Hence, the grouped averaging gives dramatically better accuracy than simply averaging  $s$ ,  $\theta$ ,  $c_f$ ,  $c_D$  individually.

### 4.3.2 Upwinding

As defined above, the governing equations are equivalent to two-point central (or ‘‘box’’) differencing, and are second-order accurate. Unfortunately this also makes them sensitive to oscillations in cases where the grid node spacing is too coarse to resolve sharp gradients in the differenced variables. This problem is most severe in the shape parameter equation (99) is stiff, in that which evolves  $H^*(s)$  with a small length scale which is comparable to  $\theta/c_f$ , which for turbulent flow can easily be much smaller than a practical grid spacing. An undershoot in  $H^*$  can easily result in  $H < 1$ , for which all the profile correlations are not defined, resulting in a solution failure.

The problem is resolved by replacing the  $c_f$  and  $c_D$  group averages with upwinded averages which bias the downstream station more. Specifically, we redefine

$$\left( \frac{s c_f}{\theta} \right)_a = \chi \left( \frac{s c_f}{\theta} \right)_{i-1} + (1-\chi) \left( \frac{s c_f}{\theta} \right)_i \quad (123)$$

$$\chi = 0.5 \dots 1 \quad (124)$$

where the upwinding parameter  $\chi$  can take on any value from 0.5 to 1 as indicated. Choosing  $\chi=0.5$  recovers the simple average with best accuracy. Choosing  $\chi > 0.5$  progressively increases the damping of oscillations while decreasing accuracy. The limiting case  $\chi = 1$  is equivalent to backward Euler, which is extremely stable but also least accurate. In the actual implementation,  $\chi$  is defined locally by the heuristic relation

$$\chi = 1 - \frac{1}{2} \exp \left[ - \left( \ln \frac{H_{k_i} - 1}{H_{k_{i-1}} - 1} \right)^2 \frac{1}{H_{k_i}^2} \right] \quad (125)$$

which introduces upwinding only where  $H_{k_i} - 1$  starts to significantly differ from  $H_{k_{i-1}} - 1$ , which indicates that a sawtooth oscillation is present.

The shear lag equation (101) is also stiff and is susceptible to oscillations in the  $C_\tau^{1/2}$  variable. Here the problem is solved by upwinded averaging of  $C_{\tau_{EQ}}^{1/2}$  and  $C_\tau^{1/2}$  in the corresponding residual (121).

### 4.3.3 Initial Conditions

All the boundary layer equations require some initial condition at the first point  $i=1$ . We also note that over the first interval from the leading edge or stagnation point, at  $i=2$ , we have  $s_{i-1} = s_1 = 0$ , and hence the equations must be modified to avoid the logarithmic singularities. Both issues are resolved by making the assumption that self-similar flow is present over the first interval. Based on Falkner-Skan theory, this assumption is equivalent to assuming that the velocity varies in a power-law manner over the first interval.

$$u_e(s) = Cs^a \quad (126)$$

The exponent  $a$  can be either assumed depending on the type of flow, or computed from the next-downstream interval.

$$a = \begin{cases} 0 & , \text{ flat-plate leading edge assumed} \\ 1 & , \text{ stagnation point leading edge assumed} \\ \frac{\ln u_{e3}/u_{e2}}{\ln s_3/s_2} & , \text{ defined from downstream interval} \end{cases} \quad (127)$$

In residuals (119) and (120) we then replace the ratio logarithms with the following values,

$$\ln \frac{s_i}{s_{i-1}} = 1 \quad (128)$$

$$\ln \frac{u_{e_i}}{u_{e_{i-1}}} = a \quad (129)$$

$$\ln \frac{\theta_i}{\theta_{i-1}} = \frac{1-a}{2} \quad (130)$$

$$\ln \frac{H_i^*}{H_{i-1}^*} = 0 \quad (131)$$

and also take the averages from the  $i=2$  station only.

$$\left( \frac{s c_f}{\theta 2} \right)_a = \left( \frac{s c_f}{\theta 2} \right)_2 \quad (132)$$

$$H_a = H_2, \quad \text{etc.} \quad (133)$$

These changes in effect convert the differential equations into algebraic relations, which then serve as implicit initial conditions on the initial  $\theta$  and  $H^*$  values at  $i=2$ .

For the first interval, we also replace the amplification equation residual (122) with the simple initial condition

$$\tilde{n}_2 = 0 \quad (134)$$

which reasonably assumes that no amplification has occurred over the first interval.

The shear lag equation residual (121) is implemented only after transition, and hence requires an initial condition at the transition location  $s_{\text{tr}}$ . At this location we impose the initial condition

$$C_\tau^{1/2} = K \tilde{C}_{\tau_{EQ}}^{1/2}(H_{k_{\text{tr}}}, Re_{\theta_{\text{tr}}}, M_{e_{\text{tr}}}) \quad (135)$$

$$K(H_{k_{\text{tr}}}) = 1.8 \exp\left(\frac{-3.3}{H_k - 1}\right) \quad (136)$$

where the  $K$  is scaling function calibrated to obtain observed pressure gradients in a separation bubble immediately downstream of transition. This has a strong effect on bubble losses and on the bubble's resistance to bursting, which is dominated by the value of  $c_{\mathcal{D}}$  and hence of  $C_{\tau}$  there. In attached flow,  $K$  has little or no effect on the solution, since the lag equation (121) quickly decays any influence of the initial value on the downstream  $C_{\tau}^{1/2}(s)$  evolution.

#### 4.3.4 Transition Point Determination

If free transition is chosen, the transition point location  $s_{\text{tr}}$  is determined by applying residual (122) to the subinterval  $s_{i-1} \cdots s_{\text{tr}}$ , and replacing  $\tilde{n}_i$  with the specified  $n_{\text{crit}}$  parameter. We then have

$$s_{\text{tr}} = s_{i-1} + \theta_a \frac{n_{\text{crit}} - \tilde{n}_{i-1}}{\mathcal{F}_n(H_{k_a}, Re_{\theta_a})} \quad (137)$$

which is still an implicit equation for  $s_{\text{tr}}$ , since the sub-interval average  $\theta_a$  depends on  $\theta_{\text{tr}}$ , which itself depends on  $s_{\text{tr}}$ .

$$\theta_{\text{tr}} = \frac{s_i - s_{\text{tr}}}{s_i - s_{i-1}} \theta_{i-1} + \frac{s_{\text{tr}} - s_{i-1}}{s_i - s_{i-1}} \theta_i \quad (138)$$

$$\theta_a = \frac{1}{2} (\theta_{i-1} + \theta_{\text{tr}}) \quad (139)$$

The  $H_{k_a}, Re_{\theta_a}$  function arguments can also be weighted averages over the sub-interval, although in practice the fully upwinded arguments

$$H_{k_a} = H_{k_{i-1}} \quad (140)$$

$$Re_{\theta_a} = Re_{\theta_{i-1}} \quad (141)$$

give the most stable solution behavior, especially on coarse grids.

If forced transition is chosen, the transition point location  $s_{\text{tr}}$  is explicitly prescribed, and equation (138) is not used. In practice, it is preferable to always compute a candidate  $s_{\text{tr}}$  from equation (138), and use this as the actual transition location if it falls upstream of the specified forced-transition location. This prevents the formation of a massive laminar separation zone and likely solution failure if separation occurs upstream of the forced-transition location.

## 4.4 Coupled Viscous/Inviscid Solution

The viscous/inviscid problem augments the full-potential problem by the addition of the four boundary layer variables and the four associated residuals for each surface and wake point. The viscous variables and residuals can be conveniently grouped into the vectors

$$v_i \equiv \left\{ \tilde{n}_i \quad \theta_i \quad m_i \quad u_{e_i} \right\}^T$$

$$\mathcal{R}_i^v \equiv \left\{ \mathcal{R}_i^n \quad \mathcal{R}_i^\theta \quad \mathcal{R}_i^H \quad \mathcal{R}_i^u \right\}^T$$

where  $\tilde{n}_i$  and  $\mathcal{R}_i^n$  would be replaced by  $C_{\tau_i}^{1/2}$  and  $\mathcal{R}_i^C$  in turbulent regions. The overall residual vector now includes the viscous residuals,

$$\vec{\mathcal{R}}_{(\Phi_j, v_j, g_l)} \equiv \begin{Bmatrix} \mathcal{R}_i^\Phi \\ \mathcal{R}_i^v \\ \mathcal{R}_k^g \end{Bmatrix} = \mathbf{0} \quad (142)$$

and the Newton iteration system now has the following form.

$$\begin{Bmatrix} \mathcal{R}_i^\Phi \\ \mathcal{R}_i^v \\ \mathcal{R}_k^g \end{Bmatrix}^n + \begin{bmatrix} A_{ij} & B_{ik} & C_{il} \\ D_{ij} & E_{ik} & F_{il} \\ G_{kj} & H_{kl} & K_{kl} \end{bmatrix}^n \begin{Bmatrix} \delta\Phi_j \\ \delta v_k \\ \delta g_l \end{Bmatrix} = \mathbf{0} \quad (143)$$

This matrix subdivision is conceptually useful, but in practice a smaller matrix bandwidth is produced if the viscous residual rows and viscous variable columns are interspersed with the potential residual rows and potential variable columns. The resulting matrix will then again have a four-block structure, as indicated by the double lines in equation (143), and will also be faster to solve.